AIP | Journal of Applied Physics

Shock response of a model structured nanofoam of Cu

F. P. Zhao, Q. An, B. Li, H. A. Wu, W. A. Goddard et al.

Citation: J. Appl. Phys. **113**, 063516 (2013); doi: 10.1063/1.4791758
View online: http://dx.doi.org/10.1063/1.4791758
View Table of Contents: http://jap.aip.org/resource/1/JAPIAU/v113/i6
Published by the American Institute of Physics.

Shock response of a model structured nanofoam of Cu

F. P. Zhao,[1,2] Q. An,[3] B. Li,[1] H. A. Wu,[1] W. A. Goddard III,[3] and S. N. Luo[2,4,a)]
[1]*Department of Modern Mechanics, University of Science and Technology of China, Hefei, Anhui 230027, People's Republic of China*
[2]*The Peac Institute of Multiscale Sciences, Chengdu, Sichuan 610064, People's Republic of China*
[3]*Materials and Process Simulation Center, California Institute of Technology, Pasadena, California 91125, USA*
[4]*Institute of Atomic and Molecular Physics, Sichuan University, Chengdu, Sichuan 610064, People's Republic of China*

(Received 7 December 2012; accepted 28 January 2013; published online 13 February 2013)

Using large-scale molecular dynamics simulations, we investigate shock response of a model Cu nanofoam with cylindrical voids and a high initial porosity (50% theoretical density), including elastic and plastic deformation, Hugoniot states, shock-induced melting, partial or complete void collapse, nanojetting, and hotspot formation. The elastic-plastic and overtaking shocks are observed at different shock strengths. The simulated Hugoniot states can be described with a modified, power-law $P-\alpha$ (pressure–porosity) model, and agree with shock experiments on Cu powders, as well as the compacted Hugoniot predicted with the Grüneisen equation of state. Shock-induced melting shows no clear signs of bulk premelting or superheating. Voids collapse via plastic flow nucleated from voids, and the exact processes are shock strength dependent. With increasing shock strengths, void collapse transits from the "geometrical" mode (collapse of a void is dominated by crystallography and void geometry and can be different from that of one another) to "hydrodynamic" mode (collapse of a void is similar to one another); the collapse may be achieved predominantly by flow along the {111} slip planes, by way of alternating compression and tension zones, by means of transverse flows, via forward and transverse flows, or through forward nanojetting. The internal jetting induces pronounced shock front roughening, leading to internal hotspot formation and sizable high speed jets on atomically flat free surfaces. [http://dx.doi.org/10.1063/1.4791758]

I. INTRODUCTION

Shock response of porous and powder materials is not only of significance for shock physics but also bears important applications to materials synthesis and engineering.[1–20] Metallic foams are of particular interest for their light weight and high stiffness,[9] and polymeric foams are useful as X-ray generators or laser ablators.[18,21] The successful synthesis of metallic foams,[22,23] in particular nanofoams,[23] offers new opportunities for exploiting their uniqueness, and motivates us to perform molecular dynamics (MD) simulations of their impact response.

While shock responses of porous and powder materials are interesting, their low densities and pronounced structural inhomogeneities often make temporally or spatially resolved measurements extremely difficult, if not impossible. Direct MD simulations of high porosity nanofoams under shock loading are still rare. Lane *et al*. recently reported MD simulations of a polymeric, poly(4-methyl-1-pentene), nanofoam with regular patterned spherical voids.[18] Our knowledge of phenomenology and mechanisms of shock response of nanofoams is limited. As a first attempt on metallic nanofoams, here we perform MD simulations of Cu nanofoams (~50% theoretical density) with structured columnar nanovoids under shock wave loading, to investigate elastic and plastic deformation, Hugoniot states, shock-induced melting, void collapse, nanojetting, and hotspot formation, as well as underlying mechanisms. The nanoscale simulations of the Hugoniot states are in accord with micro- or larger scale experiments[6] and the compacted Hugoniot predicted with the Grüneisen equation of state.[2] A modified power-law $P-\alpha$ (pressure–porosity) model[3] is proposed for low pressures. Different void collapse mechanisms are identified. Internal jetting induces hotspots and free surface jetting. We present methodology in Sec. II, and results and discussion in Sec. III, followed by conclusions in Sec. IV.

II. METHODOLOGY

We use the Large-scale Atomic/Molecular Massively Parallel Simulator (LAMMPS),[24] and an accurate embedded-atom-method potential of Cu,[25] in our MD simulations. For a porous or powder material with an initial specific volume (V_{00}), we characterize its porosity with the ratio of its specific volume at a state of interest (V) to that of the full-density solid at ambient conditions (V_0), $\alpha \equiv V/V_0$, and $\alpha_0 = V_{00}/V_0$. In this work, we focus on $\alpha_0 \approx 2$.

Nanofoams (referring loosely to high porosities) can have open- or closed-cell pore structures, and the latter is considered here. We choose columnar or cylindrical voids for their simplicity, created from a Cu [100] single crystal (Fig. 1). The void diameter is about 8 nm, and void centers form a square pattern. The x-, y-, and z-axes are along

a)sheng.n.luo@gmail.com.

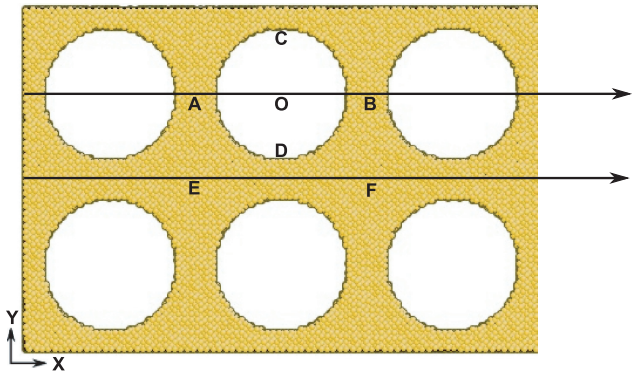

FIG. 1. Partial configuration of a Cu nanofoam created from a [100] single crystal. Shock loading is along the *x*-axis or [100].

[100], [010], and [001], respectively, and shock loading is along the *x*-direction. The *yz*-crosssection is 20 nm×5 nm, and the dimension along the shock direction is 400 nm. The system size is about 2 00 000 atoms. The configurations are relaxed and thermalized at the ambient conditions with the constant-pressure-temperature ensemble and three-dimensional (3D) periodic boundary conditions. For shock simulations, we assign an initial particle velocity, $-u_p$, along the -*x*-axis to a nanofoam, and let it impact a rigid momentum wall. The resulting shock wave propagates in the opposite direction. u_p is equivalent to the piston velocity in piston-driven shock loading. In shock simulations, periodic boundary conditions are applied only along the *y*- and *z*-axes. The time step for integration of the equation of motion is 1 fs, and the run durations are up to 250 ps. If needed, a Lennard-Jones absorbing wall is applied to the plastic wave region with the wall velocity equaling to the average particle velocity in the plastic wave region, in order to achieve long equilibration durations. No additional constraints are applied to the classical trajectories beyond the shock loading and the absorbing wall.

We perform 1D and 2D binning analyses[26,27] to resolve spatially such physical properties as density ($\rho = 1/V$), stress tensor (σ_{ij}), von Mises stress (σ_{vM}), particle velocity (u), and temperature (T) profiles at different stages of compression and release. The binning width is 5 Å or 10 Å. Averaging along the *z*-axis is applied for 2D analysis. To calculate T and σ_{ij} within each bin, we need remove its center-of-mass velocity, $\bar{v}_i$ ($i = x$, y and z), or apply corrections: $\Delta T = -(m/3k_B)(\bar{v}_x^2 + \bar{v}_y^2 + \bar{v}_z^2)$, and $\Delta\sigma_{ij} = -(Nm/V_a)\bar{v}_i\bar{v}_j$, where m is the atomic mass, V_a is the atomic volume, and N is the number of Cu atoms in the volume under consideration. We also characterize the local deformation and local structure around an atom with the local von Mises shear strain invariant (η_{vM})[28,29] and centrosymmetry parameter.[30] For shock-induced melting, the mean squared displacements (MSD) are cal culated as $\text{MSD} = \langle|\mathbf{r}(t) - \mathbf{r}(0)|^2\rangle$, where $\langle\cdots\rangle$ denotes averaging over ensemble and time origin, $\mathbf{r}$ is the atomic position, and t is the time. The diffusion coefficient (D) is related to MSD via the Einstein relation, $\text{MSD} = 6\,Dt$.

A supported shock state is characterized in terms of σ_{ij} or pressure (P), ρ or V, internal energy (E), T, shock velocity (U_s), and particle velocity (u_p). The Hugoniot jump conditions from state $i-1$ to state i for mass, momentum and energy conservations are

$$\rho_{i-1}U_{s,i} = \rho_i(U_{s,i} - u_{p,i}), \tag{1}$$

$$P_i - P_{i-1} = \rho_{i-1}(U_{s,i} - u_{p,i-1})(u_{p,i} - u_{p,i-1}), \tag{2}$$

and

$$E_i - E_{i-1} = \frac{1}{2}(P_i + P_{i-1})(V_{i-1} - V_i), \tag{3}$$

respectively. (P and σ_{xx} are used interchangeably in our discussion.) $i = 0$, 1, and 2 in current study, representing the initial state, elastic wave and plastic waves, respectively. For pure elastic shock and the cases where the plastic wave overtakes the elastic wave, the jump conditions only involve two states. The $U_s - u_p$ relation can be linear: $U_s = C_0 + su_p$, where $C_0 = 3.94$ km s^{-1} and $s = 1.5$ for full density Cu as obtained from experiments,[31] and the MD results are similar.[32]

For a full density solid, the Hugoniot centered at V_0 is

$$P_H = \frac{C_0^2(V_0 - V)}{[V_0 - s(V_0 - V)]^2}. \tag{4}$$

Different states with the same V, e.g., Hugoniots centered at V_0 and V_{00}, can be related with the Mie-Grüneisen equation in the finite difference form via the Grüneisen parameter $\gamma = V(\Delta P/\Delta E)|_V$.[1,2] Its volume dependence is normally assumed to be $\gamma_0/V_0 = \gamma/V$, and $\gamma_0 = 2$ for Cu.[2] For a porous solid (V_{00}), if we suppose that the specific volume collapses from V_{00} to V_0 instantaneously upon compression, then the theoretical compacted Hugoniot is

$$P_H = \frac{[2V - \gamma(V_0 - V)]C_0^2(V_0 - V)}{[2V - \gamma(V_{00} - V)][V_0 - s(V_0 - V)]^2}. \tag{5}$$

In special cases, where $\gamma = 2(V_{00}/V - 1)$, $P_H \to \infty$.[1,2]

There are different models for compaction of porous or powder materials, including the $P - \alpha$ model and its variations,[3,4] $P - \lambda$ model,[10] and Wu–Jing model.[8] The $P - \alpha$ model involves two critical pressures for the onset of plasticity (P_e) and full compaction (P_s). We propose a modified power-law $P - \alpha$ model with finite P_e

$$\alpha = \left(\frac{P_s - P_e}{P_H - P_e}\right)^{\frac{1}{n}}, \tag{6}$$

and it follows that

$$P_H - P_e = (P_s - P_e)\left(\frac{V_0}{V}\right)^n. \tag{7}$$

III. RESULTS AND DISCUSSION

Shock loading is applied at $u_p = 0.05 - 2.5$ km s^{-1}, generating elastic, elastic–plastic/two–wave, or overtaking shocks in the nanofoams. Shock front and the region behind

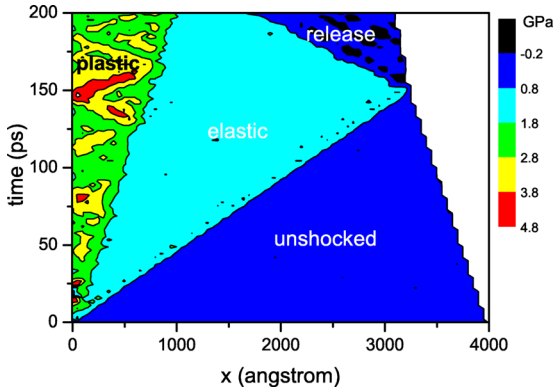

FIG. 2. The $x-t$ diagram of σ_{xx} for $u_p = 0.5$ km s^{-1}, showing different regimes: unshocked, elastic precursor, plastic wave, and elastic release.

show 2D features owing to the microstructure. From the trajectories, we perform 1D/2D binning and atomic-level structure/deformation analyses, examine elastic and plastic deformation, Hugoniot states, shock-induced melting, partial or complete void collapse, nanojetting and hotspot formation, and address both phenomenology and mechanisms. Since the majority of shock experiments assume 1D strain loading, we present 1D binning analysis first (Figs. 2–5), followed by 2D and atomic configuration analyses (Figs. 6–12).

The $x-t$ diagram ($u_p = 0.5$ km s^{-1}, Fig. 2) illustrates wave propagation during shock compression and subsequent release from the free surface: the impact induces two right-travelling shocks (the elastic precursor and plastic wave) originated from the rigid wall, and the elastic shock is then reflected by the free surface as a release fan. With the preexisting voids, the 1D analysis reveals temporal and spatial fluctuations (the "structures" in the $x-t$ diagram). Below the Hugoniot elastic limit (HEL), there exists only a single elastic shock (e.g., $u_p = 0.05$ km s^{-1}), while at sufficiently high shock strengths, the second shock overtakes the elastic shock and forms a single overtaking shock. When necessary, an absorbing wall is placed behind the second or overtaking shock front, to achieve much longer equilibration time.

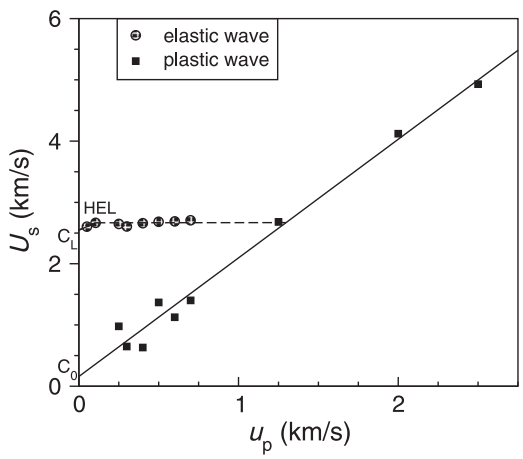

FIG. 3. The shock velocity–particle velocity ($U_s - u_p$) plot for elastic and plastic shocks. HEL: Hugoniot elastic limit. C_L (2.5 km s^{-1}) and C_0 (0.16 km s^{-1}) are the intercepts of the straight lines with the vertical axis.

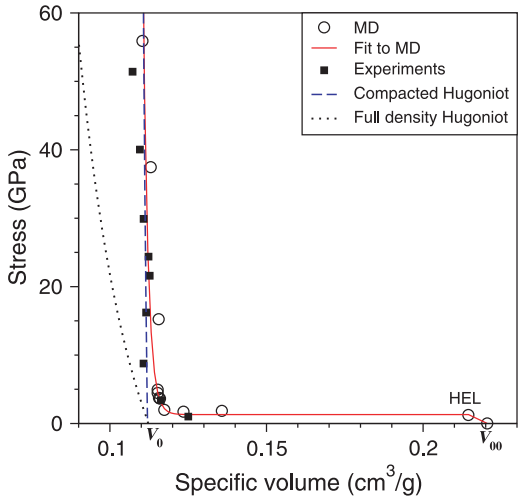

FIG. 4. The stress (σ_{xx})–specific volume (V) curves obtained from MD simulations, fit to MD results, experiments on porous and full density Cu,[6,31] and predicted compacted Hugoniot.

Direct measurements from the 1D binning analyses and calculations with the jump conditions [Eqs. (1) and (2)], allow us to obtain the usual $U_s - u_p$, and $P - V$ or $\sigma_{xx} - V$ plots (Figs. 3 and 4). The HEL is located at $u_p = 0.104$ km s^{-1} and $\sigma_{xx} = 1.27$ GPa; the corresponding $U_s = 2.67$ km s^{-1}, and $\sigma_{vM} = 0.8$ GPa. The two-wave structure regime is between HEL and $u_p = 1.25$ km s^{-1} (the overtake). The $U_s - u_p$ relations in the purely elastic and "plastic" waves can be described with linear relations, and it is $U_s = 0.16 + 1.94u_p$ in km s^{-1} for the latter. The scatter in U_s for the plastic wave at low shock strengths is due to the high porosity, as in experimental measurements.

Fitting to the simulation results with the modified power law $P - \alpha$ model [Eq. (7)] and $P_e = 1.27$ GPa yields $n \approx 64.6$, and $P_s \approx 20.6$ GPa; weighting with y^{-2} is applied

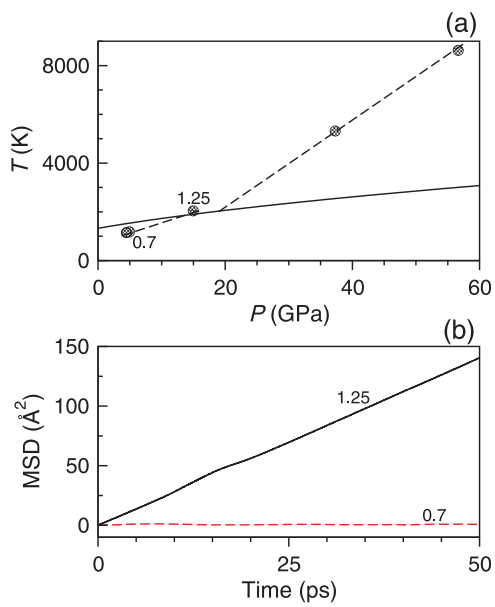

FIG. 5. (a) The shock pressure–temperature (P–T) plot for different u_p (circles), along with the equilibrium melting curve (solid curve).[32] The dashed curves are guide to the eye. (b) MSDs obtained from the absorbing wall simulations. The numbers in (a) and (b) denote u_p in km s^{-1}.

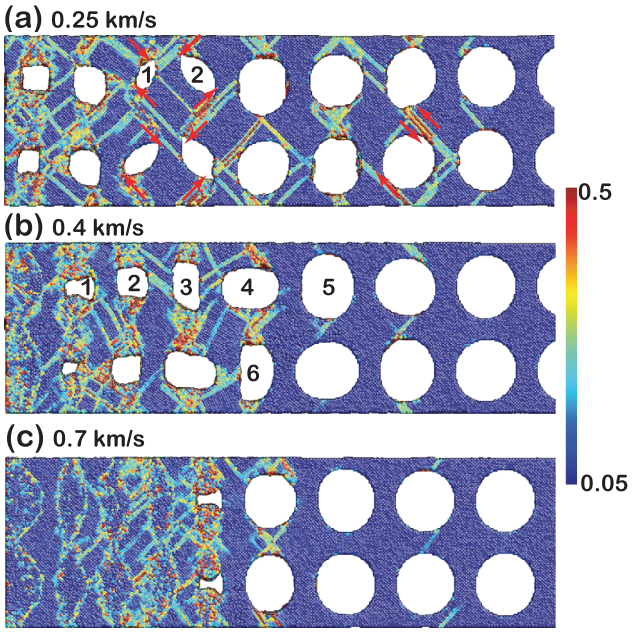

FIG. 6. Atomic configurations (projected onto the *xy*-plane) for (a) $u_p = 0.25$ km s^{-1} and $t = 100$ ps; (b) $u_p = 0.4$ km s^{-1} and $t = 50$ ps; (c) $u_p = 0.7$ km s^{-1} and $t = 37$ ps. Color-coding is based on η_{vM}. Shock direction: left → right.

to the fitting to favor the low pressure data (Fig. 4). We also plot the experimental data of Cu powders with the same α_0 (squares),[6] the full density experimental result in terms of Eq. (4) (dotted curve),[31] and the compacted Hugoniot predicted with Eq. (5) (dashed curve). The simulations, experiments, and theoretical compacted Hugoniot are in remarkable agreement at high pressures, which validates the Grüneisen formulation for porous materials. Such an

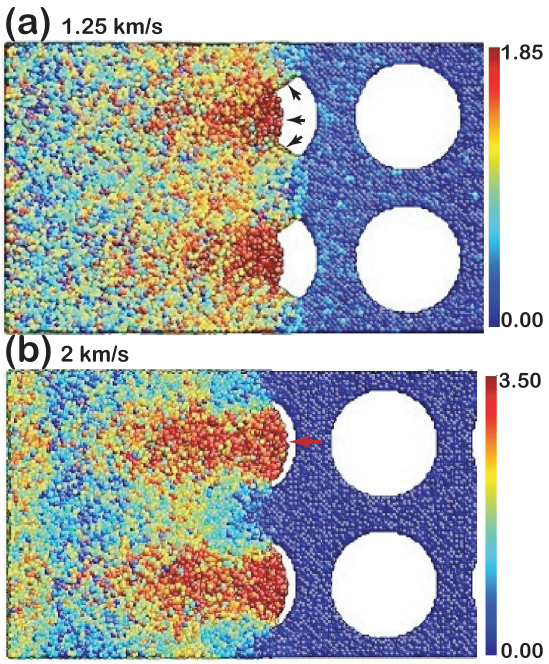

FIG. 7. Atomic configurations (projected onto the *xy*-plane) for $u_p = 1.25$ km s^{-1} and $t = 14$ ps; (b) $u_p = 2$ km s^{-1} and $t = 9$ ps, showing forward or transverse flows (arrows). Color-coding is based on u_x in km s^{-1}. Shock direction: left → right.

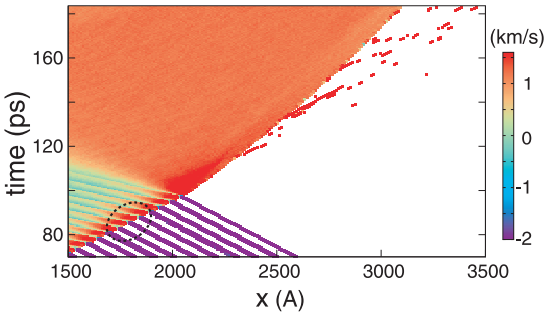

FIG. 8. The $x - t$ diagram of a 1-nm thick slice cut along the void diameter in the shock direction (*AOB* in Fig. 1) obtained from the 2D binning analysis for $u_p = 2$ km s^{-1}, showing internal jetting (circled region), free surface jetting and atomization. Color-coding is based on u_x. Shock direction: left → right.

agreement suggests that porosity is the pivotal parameter for high-pressure equation of state, and the scale effects (nanoscale in our simulations vs. micro- or larger scales in experiments) may be insignificant in this regard. The low pressure experimental data also agree with MD simulations. Supposedly, the void characteristics matter for void collapse at low pressures, but the differences in $P - V$ due to different compaction behaviors may be within measurement uncertainties. The rapid steepening of the porous $P - V$ curve relative to the full density Hugoniot is because for this particular

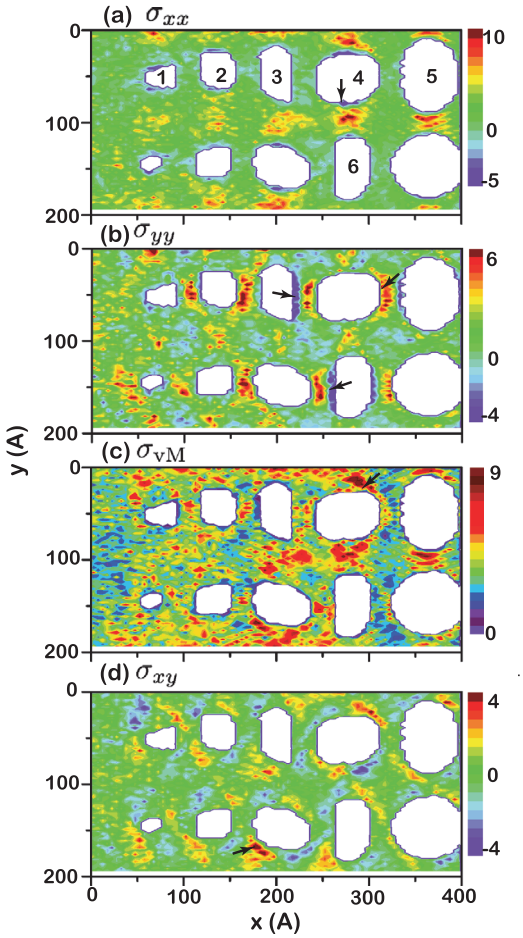

FIG. 9. 2D stress ($\sigma_{xx}, \sigma_{yy}, \sigma_{vM}$, and σ_{xy} in GPa) maps on the *xy*-plane for $u_p = 0.4$ km s^{-1} and $t = 50$ ps [cf. Fig. 6(b)]. Shock direction: left → right.

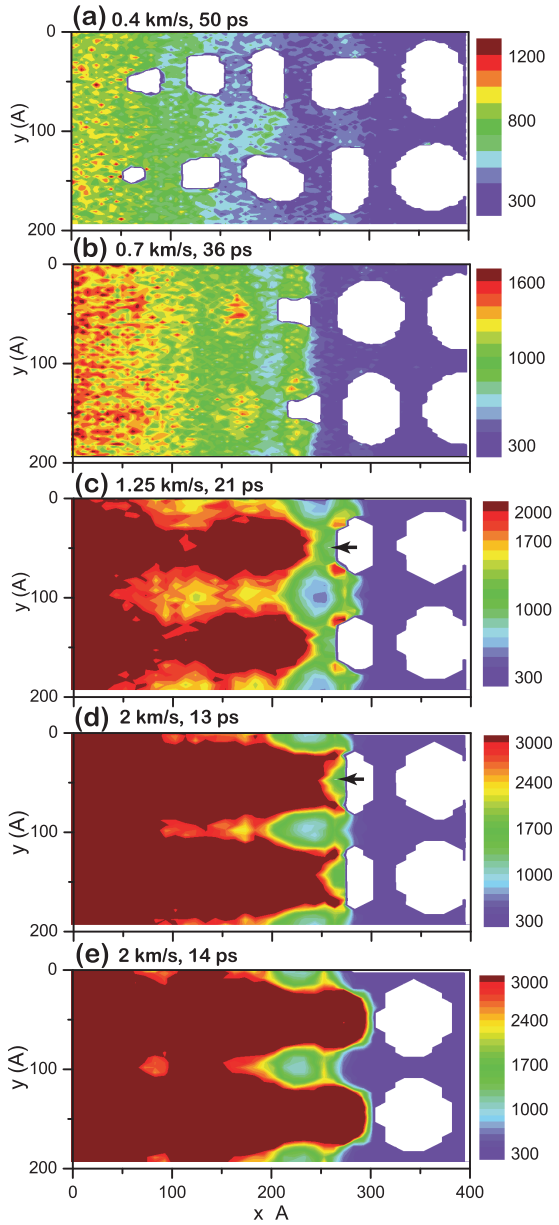

FIG. 10. 2D temperature maps on the *xy*-plane for different shock strengths, showing hotspot formation due to internal jetting. Temperature is in K. Color is saturated above a chosen temperature. Shock direction: left → right.

material (γ) and initial porosity, $P_H \to \infty$ at full compaction [cf. Eq. (5)].[1,2]

Given high initial porosities, shock-induced melting in nanofoams may occur at much lower shock strengths than in a single crystal Cu. Single crystal Cu shocked along ⟨100⟩ undergoes pronounced superheating (~20%) and melts at about 250 GPa.[32,33] The $U_s - u_p$ and $P - V$ curves do not reveal definitive signatures of melting. We thus use shock temperature and MSD[34,35] to identify melting (Fig. 5). For MSD, an absorbing wall is applied to the "plastic" wave regime. While the MSD– t curve for $u_p = 0.7$ km s^{-1} remains flat, the curve for 1.25 km s^{-1} increases linearly with time [Fig. 5(b)], indicating that the shock-compacted foam remains in a solid state for the former and melting occurs for the latter ($D \sim 5 \times 10^{-9}$ m^2 s^{-1}). Comparison of the shock temperature with the equilibrium melting curve suggests near-equilibrium, partial melting for $u_p = 1.25$ km s^{-1} [Fig. 5(a)], at much lower a shock strength than the single crystal. This can be attributed to heterogeneous melt nucleation and internal jetting (see discussion below). While bulk superheating is insignificant for $u_p = 1.25$ km s^{-1}, premelting is also absent for $u_p = 0.7$ km s^{-1}.

The 1D binning analyses presented above are certainly inadequate as regards void collapse, jetting and hotspot formation. The 2D binning and atomic-level deformation/structure analyses (Figs. 6–12) are more appropriate, and discussed next.

Similar to collapse of spherical Cu nanovoids,[12,36] quasi-2D cylindrical voids collapse via plastic flow (emission of shear loops). Complete void collapse occurs at $u_p > 0.6$ km s^{-1}. Different void deformation and collapse modes are identified at different shock strengths. At $u_p = 0.25$ km s^{-1}, the circular void shape becomes slanted ellipses, and neighboring voids along the shock direction are slanted in opposite directions [e.g., voids 1 and 2, Fig. 6(a)]. At 0.4 km s^{-1}, the voids are elongated either along or perpendicular to the shock direction, alternately between neighboring voids [e.g., voids 4 and 5, and 4 and 6, Fig. 6(b)]. With further increase in shock strength, the asymmetric collapse shifts into a "hydrodynamic" mode, where the collapse of a void is similar to one another [≥0.7 km s^{-1}, Figs. 6(c) and 7]. Both forward (along the shock direction) and transverse plastic flows contribute to void collapse; the transverse flow dominates the forward flow at lower shock strengths [0.7 km s^{-1}, Fig. 6(c)], while the forward flow becomes comparable to transverse flow [1.25 km s^{-1}, Fig. 7(a)], or outruns it and forms internal nanojets at high shock strengths [2 km s^{-1}, Figs. 7(b) and 8].

To reveal the mechanism of void collapse, we compare local atomic shear strain distributions (η_{vM}) at different shock strengths (Fig. 6). The centrosymmetry parameter analysis results are consistent, showing stacking faults (partial dislocations) and other defects. For $u_p = 0.25$ km s^{-1} [Fig. 6(a)], plastic deformation is nucleated from void edges with activated {111} slip systems. These shear zones develop, intersect, and induce relative shearing in the region between neighboring voids, which deforms a circular void into a slanted ellipse. Such partial void collapse is a direct result of the "long range" plastic flow along {111} slip planes for this particular void geometry.

At $u_p = 0.4$ km s^{-1} [Fig. 6(b)], plastic deformation is manifested as well-defined slip planes, and localized plastic zones on the top and bottom of a void where the {111} shear zone growth is frustrated; the latter feature outweighs the former. The initial void collapse is along the horizontal or vertical direction. Interestingly, this directional collapse alternates in both x- and y-directions, and can be explained in terms of 2D stress distributions. In Fig. 9(a), σ_{xx} is negative on the top and bottom of certain voids (e.g., the arrow in void 4), so the tension along the x-axis induces elongation in this direction. Similarly, the σ_{yy} map shows tension for voids 3 and 6, and compression for void 4 [the arrows in Fig. 9(b)], leading to their elongation either along or perpendicular to the y-axis. The alternating void elongation directions are a result of alternating tension and compression zones. The σ_{vM} map [Fig. 9(c)] shows concentrations on the top and bottom

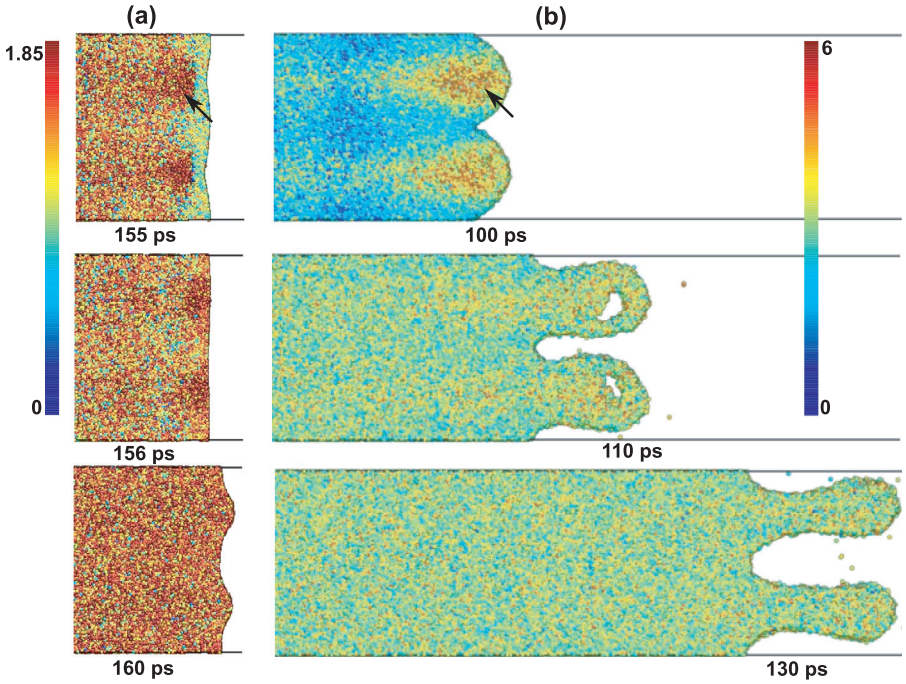

FIG. 11. Atomic configurations (projected onto the *xy*-plane) showing nanojets at free surfaces for (a) $u_p = 1.25$ km s^{-1} and (b) $u_p = 2$ km s^{-1}. Atoms are color-coded with u_x in km s^{-1}. Shock direction: left → right.

of a void, responsible for the localized deformations as opposed to long-range {111} shear zones. Around a void, there are four shear stress (σ_{xy}) zones with alternating plus and minus signs, so the void rotation is small (much less compared to the case of $u_p = 0.25$ km s^{-1}), except at locations with unbalanced shearing, for instance, the region indicated an arrow [Fig. 9(d)]. We also double the simulation cell size along the *y*-axis to examine possible size effects, and the result is similar. In the above two cases ($u_p = 0.25$ and 0.4 km s^{-1}), the void collapse mode is termed "geometrical" mode, since the collapse is due to the flow along crystallographic slip planes, or the preferential void elongation follows the stress concentrations specific for a void geometry. As a result, the early collapse of a void can be different from that of one another.

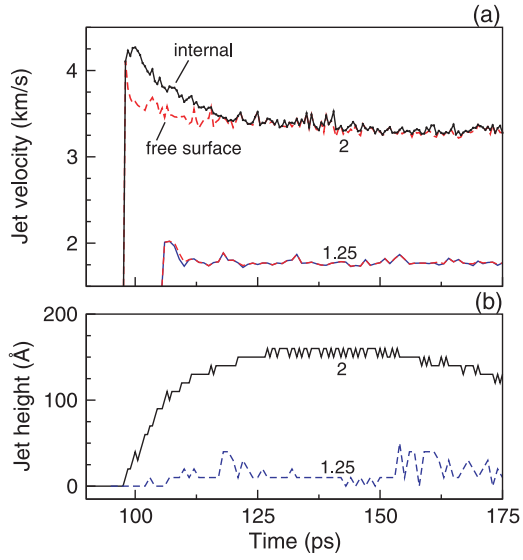

FIG. 12. Jet velocity (a) and jet height (b) for different u_p. The numbers denote u_p in km s^{-1}. The curves for $u_p = 1.25$ km s^{-1} are shifted by −50 ps.

At higher shock strengths, long-range development of {111} shear zones is further frustrated due to the high rate and high stresses, so plastic flow becomes more "hydrodynamic" (the early collapse of a void is similar to that of one another). For $u_p = 0.7$ km s^{-1}, strain concentrations are localized initially on the top and bottom of a void (near *C* and *D* in Fig. 1), so transverse flow is the dominant factor for void collapse [Fig. 6(c)]. For $u_p = 1.25$ km s^{-1}, forward flows deform the void side walls (*A* and *B* in Fig. 1), and void collapse is achieved via forward and transverse plastic flows [Fig. 7(a)]. For $u_p = 2$ km s^{-1}, the collapse is dominated by forward flows due to the formation of high speed internal jets [Figs. 7(b) and 8]; an internal jet is stopped by a side wall, and their impact leads to next internal jet.

Porous materials are prone to forming hotspots. Extra mechanical work from volume collapse and impact of high speed internal jets on matrix contribute to hotspot formation, which are of particular significance for detonation initiation in energetic materials.[37] Shock loading of metal nanofoams, in the absence of chemistry, may still shed light on hotspot formation in energetic materials. Fig. 10 shows 2D temperature maps for different shock strengths. At $u_p = 0.4$ km s^{-1}, the partial collapse of void does not induce hotspots [Fig. 10(a)], while a complete collapse at 0.7 km s^{-1} create hotspots only slightly hotter than their surroundings [Fig. 10(b)]. However, for $u_p \geq 1.25$ km s^{-1} [Figs. 10(c)–10(e)], the hotspots form along the paths of internal jetting (cf. *AB* in Fig. 1), which are considerably hotter than the region away from the voids (*EF*). Note that hotspots only form after the nanojets encounter the matrix walls, and the "free-traveling" nanojets before the impact [indicated by arrows in Figs. 10(c) and 10(d)] are colder than the hotspots. Thus, forming high speed jets and their impact with matrix are necessary for hotspot formation.

When a planar shock arrives at a free surface, preexisting suface roughness or microstructure may induce enhanced

surface roughening, surface jetting or ejecta due to differential shock breakouts and thus differential free surface velocities, a phenomenon well observed in experiments and MD simulations.[38–40] The surface roughness may seed instability and lead to instability growth (e.g., Rayleigh–Taylor and Richtmyer–Meshkov instabilities) undesirable for such processes as intertial confinement fusion.[21,38] By the same token, the non-uniformity of shock fronts may result in instability seeding and growth on atomically flat surfaces. Our simulations fall in this case: the shock front is highly structured due to partial/complete void collapse and internal jetting (Figs. 6–10), and the shock breakout on the free surface gives rise to surface roughening and jetting (Figs. 8, 11, and 12).

We characterize the dynamics of free surface roughening/jetting and its dependence on shock strength. Jetting becomes more pronounced with increasing shock strength. Both the difference in wave speeds and internal jetting contribute to surface roughening/jetting. For $u_p \leq 1.25$ km s^{-1}, the wave traversing the matrix only (*EF*, Fig. 1) travels faster than the "wave" traversing the matrix and voids (*AB*); the former wave arrives earlier at the free surface [e.g., $t = 155$ ps, Fig. 11(a)] and induces protrusion. However, the internal jets [indicated by arrow, Fig. 11(a)] catch up and create more pronounced surface protrusion (156 ps and 160 ps). At higher shock strengths, the "wave" traversing the voids outruns that traversing only the matrix via high-speed jetting, and the internal jets push the outmost matrix rapidly and form higher speed surface jets [Fig. 11(b)]. The leading edge of the surface jet moves actually slower than the atoms behind, but the velocity gradients diminish via homogenization [comparing 100 ps and 130 ps, Fig. 11(b)]. During jet growth, the velocity gradients along the *x*-direction may create tension, void nucleation, fragmentation and atomization, and the exact dynamics depend on loading, materials properties and microstructure. For $u_p = 2$ km s^{-1}, we observe transient voids and atomization (Figs. 8 and 11).

Fig. 12 quantifies the dynamics of jet leading edge, internal atoms with highest velocity, and protrusion/jet height. Upon shock breakout, the particle velocity increases rapidly to the peak and then relaxes to a steady state, similar to experimental observations.[41] For $u_p = 2$ km s^{-1}, the ratio of the particle velocity to u_p (R) is about 2 at the peak and decreases to 1.7 at the steady state; the corresponding values are 1.6 and 1.4 for 1.25 km s^{-1} [Fig. 12(a)]. The transition from the peak state to the steady state takes about 2 ps and 20 ps for 1.25 km s^{-1} and 2 km s^{-1}, respectively. These small values of R can be attributed to the steep $P - V$ curves during release, which in turn are due to significant compact densification.[42,43] The peak jet height is about 15 Å for 1.25 km s^{-1} and 155 Å for 2 km s^{-1}. (The surface jetting is negligible for $u_p < 1.25$ km s^{-1}.) Although the scaling law from nanofoams to microfoams remains to be established, our simulations suggest that suface jetting may induce considerable nonuniformity at interfaces, and lead to instability seeding and growth.

While our MD simulations of a simplest model structure bear certain general implications to shock response of porous materials, some questions remain open for future endeavors, in particular, scaling laws, foam structure (e.g., wall thickness–void diameter ratio, grain boundaries in the matrix, porosity, void geometry, pore connectivity and dimensionality), and loading rate effects.

IV. CONCLUSIONS

We have characterized the shock response of a model Cu nanofoam. The simulated Hugoniot states can be described with a modified, power-law $P - \alpha$ model, and agree with shock experiments on Cu powders, as well as the compacted Hugoniot predicted with the Grüneisen equation of state. Such agreements validates the Grüneisen formulation for porous materials, and suggest that porosity is the pivotal parameter for high-pressure equation of state, and the scale effects may be insignificant in this regard. Shock induces heterogeneous melting with no clear signs of bulk premelting or superheating. With increasing shock strengths, void collapse transits from the "geometrical" mode to "hydrodynamic" mode; the collapse may be achieved predominantly by flow along the {111} slip planes, through alternating compression and tension zones, by means of transverse flows, via forward and transverse flows, or by way of forward nanojetting. The internal jetting induces pronounced shock front roughening, leading to internal hotspot formation and sizable high speed jets on atomically flat free surfaces. Forming high speed jets and secondary impact are necessary for hotspot formation.

ACKNOWLEDGMENTS

This work was supported in part by National Science Foundation of China (11172289) and by the Fundamental Research Funds for the Central Universities of China.

[1]Ya. B. Zel'dovich and Yu. P. Raizer, *Physics of Shock Waves and High-Temperature Hydrodynamic Phenomena* (Dover, Mineola, 2002).
[2]M. A. Meyers, *Dynamic Behavior of Materials* (Wiley, New York, 1994).
[3]W. Herrmann, J. Appl. Phys. **40**, 2490 (1969).
[4]M. M. Carroll and A. C. Holt, J. Appl. Phys. **43**, 1626 (1972).
[5]B. M. Butcher, M. M. Carroll, and A. C. Holt, J. Appl. Phys. **45**, 3864 (1974).
[6]R. F. Trunin, G. V. Simakov, Y. N. Sutulov, A. B. Medvedev, B. D. Rogozkin, and Y. E. Fedorov, Sov. Phys. JETP **69**, 580 (1989).
[7]N. N. Thadhani, Prog. Mater. Sci. **37**, 117 (1993).
[8]Q. Wu and F. Q. Jing, J. Appl. Phys. **80**, 4343 (1996).
[9]S. Santosa and T. Wierzbicki, J. Mech. Phys. Solids **46**, 645 (1998).
[10]D. E. Grady, N. A. Winfree, G. I. Kerley, L. T. Wilson, and L. D. Kuhns, J. Phys. IV **10**, 15 (2000).
[11]S. L. Lopatnikov, B. A. Gama, M. J. Haque, C. Krauthauser, and J. W. Gillespie, Jr., Int. J. Impact Eng. **30**, 421 (2004).
[12]P. Erhart, E. M. Bringa, M. Kumar, and K. Albe, Phys. Rev. B **72**, 052104 (2005).
[13]J. P. Borg, J. R. Cogar, A. Lloyd, A. Ward, D. Chapman, K. Tsembelisc, and W. G. Proud, Int. J. Impact Eng. **33**, 109 (2006).
[14]C. Dai, D. Eakins, N. Thadhani, and J. P. Liu, Appl. Phys. Lett. **90**, 071911 (2007).
[15]N. K. Bourne, K. Bennett, A. M. Milne, S. A. MacDonald, J. J. Harrigan, and J. C. F. Millett, Scr. Mater. **58**, 154 (2008).
[16]A. G. Xu, G. C. Zhang, H. Li, Y. J. Ying, and J. S. Zhu, Comput. Math. Appl. **61**, 3618 (2011).
[17]Q. Wei, H. W. Xu, X. H. Yu, T. Shimada, M. S. Rearick, D. D. Hickmott, Y. S. Zhao, and S. N. Luo, J. Appl. Phys. **110**, 056102 (2011).
[18]J. M. D. Lane, G. S. Grest, A. P. Thompson, K. R. Cochrane, M. P. Desjarlais, and T. R. Mattsson, "Shock Compression of Condensed Matter–2011," AIP Conf. Proc. **1426**, 1435 (2012).
[19]P. Song, L.-C. Cai, Q.-S. Wang, X.-M. Zhou, X. Li, Y. Zhang, S. Yuan, J.-D. Weng, and J.-B. Li, J. Appl. Phys. **110**, 103522 (2011).

[20]L. Huang, W. Z. Han, Q. An, W. A. Goddard III, and S. N. Luo, J. Appl. Phys. **111**, 013508 (2012).
[21]R. L. McCrory, R. E. Bahr, R. Betti, T. R. Boehly, T. J. B. Collins, R. S. Craxton, J. A. Delettrez, W. R. Donaldson, R. Epstein, J. Frenje, V. Y. Glebov, V. N. Goncharov, O. V. Gotchev, R. Q. Gram, D. R. Harding, D. G. Hicks, P. A. Jaanimagi, R. L. Keck, J. H. Kelly, J. P. Knauer, C. K. Li, S. J. Loucks, L. D. Lund, F. J. Marshall, P. W. McKenty, D. D. Meyerhofer, S. F. B. Morse, R. D. Petrasso, P. B. Radha, S. P. Regan, S. Roberts, F. Seguin, W. Seka, S. Skupsky, V. A. Smalyuk, C. Sorce, J. M. Soures, C. Stoeckl, R. P. J. Town, M. D. Wittman, B. Yaakobi, and J. D. Zuegel, Nucl. Fusion **41**, 1413 (2001).
[22]A. H. Brothers and D. C. Dunand, MRS Bull. **32**, 639 (2007).
[23]B. C. Tappan, S. A. Steiner, and E. P. Luther, Angew. Chem., Int. Ed. Engl. **49**, 4544 (2010).
[24]S. Plimpton, J. Comp. Phys. **117**, 1 (1995).
[25]Y. Mishin, M. J. Mehl, D. A. Papaconstantopoulos, A. F. Voter, and J. D. Kress, Phys. Rev. B **63**, 224106 (2001).
[26]S. N. Luo, Q. An, T. C. Germann, and L. B. Han, J. Appl. Phys. **106**, 013502 (2009).
[27]S. N. Luo, T. C. Germann, and D. L. Tonks, J. Appl. Phys. **107**, 123507 (2010).
[28]F. Shimizu, S. Ogata, and J. Li, Mater. Trans. **48**, 2923 (2007).
[29]J. Li, Modell. Simul. Mater. Sci. Eng. **11**, 173 (2003).
[30]C. L. Kelchner, S. J. Plimpton, and J. C. Hamilton, Phys. Rev. B **58**, 11085 (1998).
[31]S. P. Marsh, *LASL Shock Hugoniot Data* (University of California Press, Berkely, 1980).
[32]Q. An, S. N. Luo, L.-B. Han, L. Q. Zheng, and O. Tschauner, J. Phys.: Condens. Matter **20**, 095220 (2008).
[33]S. N. Luo, T. J. Ahrens, T. Çağ in, A. Strachan, W. A. Goddard III, and D. C. Swift, Phys. Rev. B **68**, 134206 (2003).
[34]L. B. Han, Q. An, R. S. Fu, L. Q. Zheng, and S. N. Luo, Physica B **405**, 748 (2010).
[35]A. M. He, S. Q. Duan, J.-L. Shao, P. Wang, and C. S. Qin, J. Appl. Phys. **112**, 074116 (2012).
[36]L. P. Dávila, P. Erhart, E. M. Bringa, M. A. Meyers, V. A. Lubarda, M. S. Schneider, R. Becker, and M. Kumar, Appl. Phys. Lett. **86**, 161902 (2005).
[37]F. P. Bowden and Y. D. Yoffe, *Initiation and Growth of Explosion in Liquids and Solids* (Cambridge University Press, Cambridge, 1952).
[38]E. N. Loomis, S. R. Greenfeld, R. P. Johnson, J. A. Cobble, S. N. Luo, and D. S. Montgomery, Phys. Plasma **17**, 056308 (2010).
[39]O. Durand and L. Soulard, J. Appl. Phys. **111**, 044901 (2012).
[40]S. N. Luo, T. C. Germann, D. L. Tonks, and Q. An, J. Appl. Phys. **108**, 093526 (2010).
[41]Y. Chen, H. Hu, T. Tang, G. Ren, Q. Li, R. Wang, and W. T. Buttler, J. Appl. Phys. **111**, 053509 (2012).
[42]J. M. Walsh and R. H. Christian, Phys. Rev. **97**, 1544 (1955).
[43]S. N. Luo, L.-B. Han, Y. Xie, Q. An, L. Q. Zheng, and K. Xia, J. Appl. Phys. **103**, 093530 (2008).